

# Dynamic modeling of a sliding ring on an elastic rod with incremental potential formulation

Weicheng Huang<sup>a</sup>, Peifei Xu<sup>a,\*</sup>, Huaiwu Zou<sup>b</sup>, Hanwu Liu<sup>b</sup>, Wenmiao Yang<sup>b</sup>, Zhaowei Liu<sup>c,\*</sup>

<sup>a</sup>*School of Mechanical Engineering, Southeast University,  
Nanjing, 211189, People's Republic of China*

<sup>b</sup>*Shanghai Institute of Aerospace Systems Engineering,  
Shanghai 201108, People's Republic of China*

<sup>c</sup>*College of Mechanics and Materials, Hohai University,  
Nanjing 211100, People's Republic of China*

---

## Abstract

Mechanical interactions between rigid rings and flexible cables are widespread in both daily life (hanging clothes) and engineering system (closing a tether-net). A reduced-order method for the dynamic analysis of sliding rings on a deformable one-dimensional (1D) rod-like object is proposed. In contrast to discretize the joint rings into multiple nodes and edges for contact detection and numerical simulation, a single point is used to reduce the order of the numerical model. In order to achieve the non-deviation condition between sliding ring and flexible rod, a novel barrier functional is derived based on incremental potential theory, and the tangent frictional interplay is later procured by a lagged dissipative formulation. The proposed barrier functional and the associated frictional functional are  $C^2$  continuous, hence the nonlinear elastodynamic system can be solved variationally by an implicit

---

\*Corresponding author

Email address: [xupeifei@seu.edu.cn](mailto:xupeifei@seu.edu.cn), [zhaowei.liu@hhu.edu.cn](mailto:zhaowei.liu@hhu.edu.cn) (Zhaowei Liu)

time-stepping scheme. The numerical framework is first applied to simple examples where the analytical solutions are available for validation. Then, multiple complex practical engineering examples are considered to showcase the effectiveness of the proposed method. The simplified ring-to-rod interaction model can provide lifelike visual effect for picture animations, and also can support the optimal design for space debris removal system.

*Keywords:* Geometric nonlinearity, Structural dynamics, Discrete model, Contact mechanics

---

## 1. Introduction

Sliding rings on a flexible rod is a commonly used structure in daily life, such as clotheslines and freight transport. The relevant research can be traced back to the last century [1, 2, 3]. Moreover, due to its high efficiency for structural connections, the ring-rod mechanism is also widely used in practical engineering, including cable-driven system [4], deployable structures [5, 6], drive belts [5, 7], and continuum manipulators/robots [8, 9]. Especially, the space tether-net system [10, 11], a novel lightweight and cost-efficient technique for space debris removal [12, 13, 14, 15], usually employs several joint rings to connect tether rods and flexible nets, in order to achieve the closing mechanism in the post-capture phase [16, 17, 18]. The core of the design of engineering structures, including bridges, railways, cable cars, and tether-net, is a mathematical model that can efficiently describe the nonlinear dynamic interaction between a flexible medium and a moving ring.

On the one side, plenty of investigations have been conducted on the mechanical modeling of rigid particles, flexible rods, and their interactions. The

dynamics of a single point mass is straightforward, i.e., its equation of motion can be given directly by using Newtonian mechanics; while the governing equations for 1D rods would be slightly more complicated, as the structural slenderness may cause geometrically nonlinear deformation. To reveal the nonlinear mechanics of slender structures when experiencing finite deflections and rotations, tremendous numerical algorithms have been developed for engineering usages over the past few decades, such as Finite Element Method (FEM) [19], Geometrically Exact Beam Formulation (GEBF) [20, 21], Absolute Nodal Coordinate Formulation (ANCF) [22, 23, 24], and Isogeometric Collocation Methods (ICM) [25]. Moving forward, even not exactly identical, the interplay between rigid rings and flexible rods can be partially treated as a sliding beam problem (e.g., classical sliding spaghetti) [26, 27], and the dynamic governing equations can be derived using Lagrangian equations with non-material volume [28, 29], extended Hamilton’s principle [30, 31], and Arbitrary Lagrangian-Eulerian (ALE) formulation [32]. As for the sliding coupling between joint ring and flexible medium, most of previous works only considered the frictionless scenario. Munoz and Jelenic formulated the sliding joint using the master-slave approach to establish the frictionless contact condition with the minimum-set coordinates [33]. Lee et al. developed a three-dimensional (3D) sliding joint for nonlinear beams concerning the discontinuity using finite element discretization [34]. An ANCF-ALE coupled framework was proposed by Hong et al. to analysis the frictionless interaction between sliding joint and flexible beam [35]. Recently, isogeometric interpolation was used for frictionless sliding contact coupling dynamics to achieve higher smoothness and strong robustness [36].

On the other side, visual animations for elastodynamic systems in computer-aided geometric design (CAGD) community usually employ another type of numerical frameworks – Discrete Differential Geometry (DDG) methods, for its robustness and computational efficiency in simulating thin elastic structures with geometrically nonlinear deformation, frictional contact [37], and fluid-structure interaction [38], such as hair fluttering and cloth wrinkling. The numerical simulation based DDG method first discretize a smooth structure into a mass-spring-damper system, while preserving its key geometric properties to capture the nonlinear deformations [39]. Previous DDG based numerical frameworks have shown surprising performance in simulating thin elastic structures, such as rods [40, 41], ribbons [42, 43, 44], plates/shells [45, 46, 47], and gridshells/nets [48, 49, 50]. Moreover, in order to be employed in mechanical/civil/aerospace engineering communities, a large number of tabletop experiments have been recently conducted to verify the correctness of those eye-catching simulations, e.g., coiling of rods [51], large deflection of strips [52], bifurcation of plates [47], and form-finding of gridshells [53]. As for the contact mechanics of flexible multibody system, incremental potential method developed in 2020 is regarded as one of the most efficient frameworks [54]. The incremental potential formulation begins with the introduction of a  $C^2$  continuous barrier functional based on the Euclidean distance between two approaching particles (or other geometric elements, e.g, edges and surfaces [55]), and derive its gradient vector (associated with repulsive force) and Hessian matrix (associated with tangential stiffness) in an analytical approach. The frictional force, similarly, is given by maximal dissipation principle with a velocity-related normalized parameter

to increase functional continuous. The incremental potential model and its extension have already shown powerful performance when dealing with complex rod-to-rod interaction problems, e.g., knot tying [56], slinky toy [57], and flagella bundling [58]. However, if both the ring and the rod are discretized into nodes and edges and they are simulated using an established rod-to-rod interaction model, the computational time is still significant due to the additional degrees of freedom. Moreover, when the ring size is small, a denser mesh and a shorter time step are needed for contact detection and numerical stability.

This manuscript aims to develop a reduced-order method for analysing the nonlinear dynamic interaction between a sliding ring on a flexible cable. Different from the conventional contact mechanics, which discretizes the ring into nodes and edges to achieve penetration detection and intersection-free dynamics, the ring in the present approach is treated as a single point for model order reduction. The non-penetration condition between a sliding joint and an elastic rod is transformed into a non-deviation condition using a novel barrier-like energy functional. It is worth noting that the barrier functional for ring-to-rod interaction is based on an incremental potential formulation with  $C^2$  continuity, such that its gradient vector and Hessian matrix are available and the flexible multibody system can be solved variationally through an implicit time-stepping method [54]. The tangential frictional interaction is implemented based on the maximal dissipation principle in a manner similar to the normal contact formulation [59]. To demonstrate the correctness and accuracy of our numerical implementation, our discrete simulation is first applied to simple examples – a sliding ring on a rigid bar (both straight

and curved), because their analytical solutions of which are available. Then, the stiffness of 1D medium is decreased to address the nonlinear dynamic coupling between a sliding ring and a deformable rod, in which the geometrically nonlinear deformation is considered. Moving forward, two complex examples with potential applications in both computer graphics (hanging clothes) and aerospace engineering (closing a tether-net) are demonstrated in order to showcase that our well-established model can solve practical engineering problems.

The remainder of this manuscript is organized as follows. In Sec. 2, the ring-to-rod contact model and the associated numerical framework are formulated in detail. The proposed numerical framework is applied onto multiple examples in Sec. 3. Finally, conclusive remarks and future research are discussed in Sec. 4.

## 2. Numerical model

In this section, we introduce a numerical model for the contact simulation between a sliding ring and a flexible rod by a modified incremental potential method. The DDG-based models for rod and plate structures are first reviewed briefly, followed by the discussion of classical incremental potential formulation for particle-particle contact. This framework is next extended for the reduced-order modeling of ring-to-rod interaction. Finally, the dynamic governing equations of motion for elastodynamic system is presented.

### 2.1. Discrete models for thin elastic structures

The DDG-based numerical frameworks for both 1D rod structures [40, 41] and 2D plate objects [60, 61] are briefly reviewed here. They have been

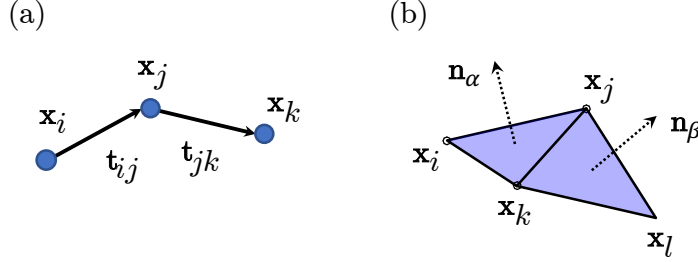


Figure 1: Discrete elements used in our numerical simulations. (a) Rod model. (b) Plate model.

validated against either experiments or analytical solutions [51, 18, 47]. The simulation domain is discretized into multiple nodes and elements and treated as a mass-spring-damper system with a lumped mass located as each vertex and the associated discrete energies. Referring to Fig. 1(a), the basic rod element combines 3 vertices,  $\mathcal{R}_{ijk} := (\mathbf{x}_i, \mathbf{x}_j, \mathbf{x}_k) \in \mathbb{R}^9$  with 2 edges, which are defined by

$$\mathbf{e}_{ij} = \mathbf{x}_j - \mathbf{x}_i, \quad (1a)$$

$$\mathbf{e}_{jk} = \mathbf{x}_k - \mathbf{x}_j, \quad (1b)$$

$$\mathbf{t}_{ij} = \frac{\mathbf{e}_{ij}}{|\mathbf{e}_{ij}|}, \quad (1c)$$

$$\mathbf{t}_{jk} = \frac{\mathbf{e}_{jk}}{|\mathbf{e}_{jk}|}, \quad (1d)$$

$$\Delta l_{ijk} = \frac{1}{2}(|\mathbf{e}_{ij}| + |\mathbf{e}_{jk}|). \quad (1e)$$

For a 1D rod with Young's modulus  $E$ , cross section area  $A$ , and moment of inertia  $I$ , the simplified discrete elastic energies are given by [18]

$$E_{\mathcal{R}}^s = \sum_{ij} \frac{1}{2} EA \frac{(|\mathbf{e}_{ij}| - |\bar{\mathbf{e}}_{ij}|)^2}{|\bar{\mathbf{e}}_{ij}|}, \quad (2a)$$

$$E_{\mathcal{R}}^b = \sum_{ijk} \frac{1}{2} EI \frac{(|\mathbf{t}_{ij} - \mathbf{t}_{jk}|)^2}{\Delta \bar{l}_{ijk}}, \quad (2b)$$

where a bar on the top represents the quantity in reference configuration. The twisting energy of rod centerline is ignored here and can be easily included by introducing one more DOF (twisting angle) if necessary [40, 41].

The plate element is defined by 4 vertices,  $\mathcal{P}_{ijkl} := (\mathbf{x}_i, \mathbf{x}_j, \mathbf{x}_k, \mathbf{x}_l) \in \mathbb{R}^{12}$  with 2 triangular faces, which are given by

$$\mathbf{e}_{ij} = \mathbf{x}_j - \mathbf{x}_i, \quad (3a)$$

$$\mathbf{e}_{ik} = \mathbf{x}_k - \mathbf{x}_i, \quad (3b)$$

$$\mathbf{e}_{lj} = \mathbf{x}_j - \mathbf{x}_l, \quad (3c)$$

$$\mathbf{e}_{lk} = \mathbf{x}_k - \mathbf{x}_l, \quad (3d)$$

$$\mathbf{t}_{ij} = \frac{\mathbf{e}_{ij}}{|\mathbf{e}_{ij}|}, \quad (3e)$$

$$\mathbf{t}_{ik} = \frac{\mathbf{e}_{ik}}{|\mathbf{e}_{ik}|}, \quad (3f)$$

$$\mathbf{t}_{lj} = \frac{\mathbf{e}_{lj}}{|\mathbf{e}_{lj}|}, \quad (3g)$$

$$\mathbf{t}_{lk} = \frac{\mathbf{e}_{lk}}{|\mathbf{e}_{lk}|}, \quad (3h)$$

$$\mathbf{n}_\alpha = \mathbf{t}_{ik} \times \mathbf{t}_{ij}, \quad (3i)$$

$$\mathbf{n}_\beta = \mathbf{t}_{lj} \times \mathbf{t}_{lk}, \quad (3j)$$

where  $\mathbf{n}_\alpha$  and  $\mathbf{n}_\beta$  are the surface normal vectors of the two triangular faces, referring to Fig. 1(b). For a 2D plate with Young's modulus  $Y$  and thickness

$b$ , the discrete elastic energies are the sum of in-plane stretching and out-of-plane bending [61],

$$E_{\mathcal{P}}^s = \sum_{ij} \frac{\sqrt{3}}{4} Y b (|\mathbf{e}_{ij}| - |\bar{\mathbf{e}}_{ij}|)^2, \quad (4a)$$

$$E_{\mathcal{P}}^b = \sum_{\alpha\beta} \frac{1}{12\sqrt{3}} Y b^3 (|\mathbf{n}_\alpha - \mathbf{n}_\beta|)^2. \quad (4b)$$

## 2.2. Incremental potential method for contact

Incremental potential contact is an efficient numerical model for nonlinear elastodynamic systems with contact [54]. Only particle-particle contact is considered in present method, and other arbitrary dimension (surfaces and curves) contact can be derived in a similar approach [55].

When the Euclidean distance between two approaching nodes,  $\mathcal{C}_{ij} := (\mathbf{x}_i, \mathbf{x}_j) \in \mathbb{R}^6$ , is smaller than a threshold, the repulsive force needs to be included into the discrete dynamic system thus the non-penetration condition can be achieved. The incremental potential model uses a nonlinear barrier-type potential with  $C^2$  continuity to achieve the intersection free condition between two approaching nodes [54],

$$E_{\mathcal{C}} = \begin{cases} -K_{\mathcal{C}} \left[ (d - \hat{d})^2 \log\left(\frac{d}{\hat{d}}\right) \right] & \text{when } 0 < d < \hat{d} \\ 0 & \text{when } d \geq \hat{d}, \end{cases} \quad (5)$$

where  $d = |\mathbf{x}_j - \mathbf{x}_i|$  is the Euclidean distance between two considered nodes,  $K_{\mathcal{C}}$  is the stiffness parameter, and  $\hat{d}$  is a barrier parameter. It is assumed here that the particle size is zero, and the relative distance can be easily derived by subtracting the particle radius if the ball with finite size is considered. By taking the variation of nonlinear barrier potential, the contact force along

the normal direction is given by [54],

$$|\mathbf{F}_C^n| = \begin{cases} K_C \left[ 2(d - \hat{d}) \log(\frac{d}{\hat{d}}) + \frac{(d - \hat{d})^2}{d} \right] & \text{when } 0 < d < \hat{d} \\ 0 & \text{when } d \geq \hat{d}. \end{cases} \quad (6)$$

The contact force is zero when the distance is beyond the threshold,  $\hat{d}$ , and would gradually increase as the distance between two nodes is smaller. The dependency of normalized contact force,  $|\mathbf{F}_C^n|/K_C$ , on the relative distance,  $d$ , for different barrier parameter,  $\hat{d} \in \{0.50, 0.75, 1.00\}$ , is plotted in Fig. 2(a).

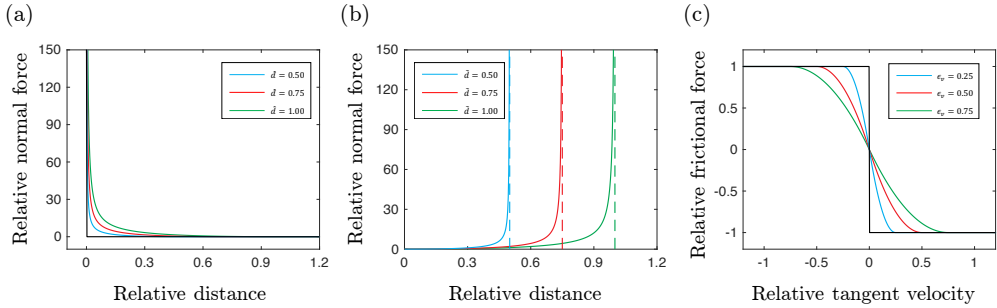


Figure 2: (a) Barrier potential for classical contact problem. (b) Modified barrier potential for the interaction between a ring and a rod. (c) Friction potential.

Then, the tangential component of contact force is applied through a dissipative potential form, which follows the maximal dissipation principle [59, 54],

$$|\mathbf{F}_C^t| = \begin{cases} \mu |\mathbf{F}_C^n| \left( -\frac{|\mathbf{v}^t|^2}{\epsilon_v^2} + \frac{|\mathbf{v}^t|}{\epsilon_v} \right) & \text{when } 0 \leq |\mathbf{v}^t| \leq \epsilon_v, \\ \mu |\mathbf{F}_C^n| & \text{when } |\mathbf{v}^t| > \epsilon_v, \end{cases} \quad (7)$$

where  $\mu$  is the frictional coefficient,  $\mathbf{v}^t$  is the relative velocity along the tangential direction between two reference nodes, and  $\epsilon_v$  is the velocity magni-

tude bound, and below which the sliding velocity is treated as static. The dependency of normalized tangential frictional force,  $|\mathbf{F}_C^t|/\mu|\mathbf{F}_C^n|$ , on the relative tangential velocity,  $|\mathbf{v}^t|$ , for different velocity bound,  $\epsilon_v \in \{0.25, 0.50, 0.75\}$ , is plotted in Fig. 2(c). This numerical treatment can smooth the discontinuity between the static friction and the dynamic friction, such that the elastodynamic system can be solved variationally.

### 2.3. Ring-to-rod contact

The conventional incremental potential formulation could handle the interaction between a ring and a rod if they are both discretized into nodes and edges. However, the redundant nodal number would slow down the overall computational efficiency. Thus, a novel barrier functional is introduced here to handle the interaction between a rigid ring and a flexible rod.

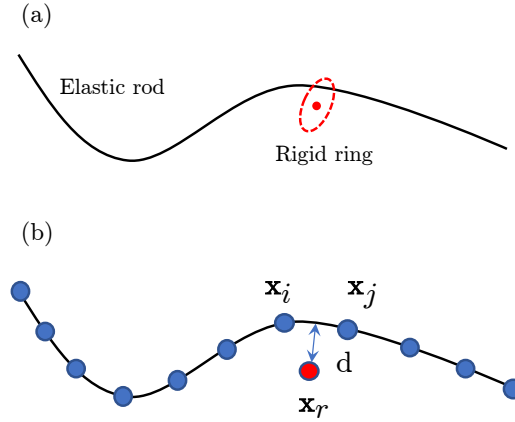


Figure 3: Problem description. (a) A rigid ring slides on a flexible rod. (b) Discrete representation.

As shown in Fig. 3, an entangled ring-rod coupled system is considered, and the rod is represented by multiple nodes while the ring is only a single

vertex. The contact element is constructed based on the minimum distance between the sliding ring and the deformable rod, and 3 nodes are considered here,  $\mathcal{J}_{i,j,r} := (\mathbf{x}_i, \mathbf{x}_j, \mathbf{x}_r) \in \mathbb{R}^9$ , where  $\mathbf{x}_i$  and  $\mathbf{x}_j$  are the vertices on rod, and  $\mathbf{x}_r$  represents the position of sliding ring. The minimum distance  $d$  between the joint and the cable here is defined by

$$d = \min\{|\mathbf{x}_r - \mathbf{x}_i|, |\mathbf{x}_r - \mathbf{x}_j|, \frac{|(\mathbf{x}_r - \mathbf{x}_i) \times (\mathbf{x}_r - \mathbf{x}_j)|}{|\mathbf{x}_j - \mathbf{x}_i|}\}. \quad (8)$$

To ensure the non-deviation condition between the sliding joint and the flexible cable, the following barrier energy functional is constructed by

$$E_{\mathcal{J}} = \begin{cases} K_{\mathcal{J}} \left[ d^2 \log(1 - \frac{d}{\tilde{d}}) \right] & \text{when } 0 < d < \tilde{d} \\ +\infty & \text{when } d \geq \tilde{d} \end{cases}, \quad (9)$$

where  $K_{\mathcal{J}}$  is the stiffness parameter and  $\tilde{d}$  is a barrier parameter similar to the  $\hat{d}$  in Eq.(6). Correspondingly, the ring radius here is assumed to be zero, and the ring-to-rod distance can be simply modified by minus the ring radius. It should also be noted that the ring-rod coupled element  $\mathcal{J}_{i,j,r}$  would update with time when the minimum distance between the moving ring and deformable rod is changed. Again, This newly introduced barrier function for ring-to-rod model is also with  $C^2$  continuous, and the normal contact force is close to zero when the distance is small, while the force is almost infinite when the distance is close to the threshold,  $\tilde{d}$ ,

$$|\mathbf{F}_{\mathcal{J}}^n| = \begin{cases} K_{\mathcal{J}} \left[ 2d \log(1 - \frac{d}{\tilde{d}}) + \frac{d^2}{d - \tilde{d}} \right] & \text{when } 0 < d < \tilde{d} \\ +\infty & \text{when } d \geq \tilde{d} \end{cases}. \quad (10)$$

With this barrier functional, the non-deviation condition between sliding ring joint and elastic cable is successfully achieved. The dependency of normalized

interaction force,  $|\mathbf{F}_{\mathcal{J}}^n|/K_{\mathcal{J}}$ , on the relative distance,  $d$ , for different barrier parameter,  $\tilde{d} \in \{0.50, 0.75, 1.00\}$ , is plotted in Fig. 2(b). The formulation of frictional force for ring-to-rod contact is identical to Eq.(7).

#### 2.4. Equations of motion

This section discusses the time marching scheme for elastodynamic system with non-penetration contact and ring-to-rod interaction. An elastic structure is discretized into  $N$  nodes and treated as a multibody dynamic system, with degrees of freedom  $\mathbf{q} \in \mathbb{R}^{3N}$ . Its second order dynamic growing equations of motion is,

$$\mathbb{M}\ddot{\mathbf{q}}(t) + \mathbb{C}\dot{\mathbf{q}}(t) + \mathbb{K}\mathbf{q}(t) = \mathbf{F}_{\text{ext}}(t), \quad (11)$$

where  $\mathbb{M}$  is the time-invariant  $3N \times 3N$  diagonal mass matrix,  $\mathbb{K} = \nabla^2 E$  (where  $E$  is the total elastic potential) is the tangential stiffness matrix,  $\mathbb{C} = \alpha\mathbb{M} + \beta\mathbb{K}$  is the Rayleigh damping matrix, and  $\mathbf{F}_{\text{ext}}$  is the external force vector (such as the gravity). Notice that the system is nonlinear, i.e.,  $\mathbb{C}$  and  $\mathbb{K}$  are time variant.

To achieve the non-penetration condition between two approaching nodes as well as the non-deviation condition between sliding joint and elastic rod, the incremental potential and the dissipative friction need to be included. Geometric detect is updated at each time step to compute  $\mathbf{F}_c$  (for particle-particle contact) and  $\mathbf{F}_{\mathcal{J}}$  (for ring-to-rod interaction). Here, the normal contact force,  $\mathbf{F}_c^n$  (and  $\mathbf{F}_{\mathcal{J}}^n$ ), is treated as a position-dependent elastic force, while the tangential friction force,  $\mathbf{F}_c^t$  (and  $\mathbf{F}_{\mathcal{J}}^t$ ), is considered as a velocity-dependent damping force.

The implicit Euler method is used to numerically update the DOF vector and its velocity from time step  $t_k$  to  $t_{k+1} = t_k + h$  ( $h$  is the time step size) [62]:

$$\mathbb{M}\ddot{\mathbf{q}}(t_{k+1}) = \mathbf{F}_{\text{int}}(t_{k+1}) + \mathbf{F}_{\mathcal{C}}(t_{k+1}) + \mathbf{F}_{\mathcal{J}}(t_{k+1}) + \mathbf{F}_d(t_{k+1}) + \mathbf{F}_g(t_{k+1}) \quad (12a)$$

$$\mathbf{q}(t_{k+1}) = \mathbf{q}(t_k) + h\dot{\mathbf{q}}(t_{k+1}) \quad (12b)$$

$$\dot{\mathbf{q}}(t_{k+1}) = \dot{\mathbf{q}}(t_k) + h\ddot{\mathbf{q}}(t_{k+1}) \quad (12c)$$

where  $\mathbf{F}_{\text{int}} = -\nabla E$  is the internal elastic force,  $\mathbf{F}_d = \mathbb{C}\dot{\mathbf{q}}$  is the damping force vector, and  $\mathbf{F}_g$  is the external gravity force vector.

As the interaction potential is based on a  $C^2$  continuous formulation, Newton-Raphson is adopted to solve the nonlinear equations of motion, e.g., the Jacobian matrix associated with Eq.(12) is available. It is important to note that the damping force and frictional force are treated semi-implicit, i.e., to get the viscoelastic damping force at  $t_{k+1}$ , the component of Rayleigh damping matrix,  $\mathbb{K}$  is evaluated at time  $t = t_k$ , while the velocity,  $\dot{\mathbf{q}}$ , is evaluated at time  $t = t_{k+1}$ ; to get the tangential frictional force at  $t_{k+1}$ , the normal contact,  $\mathbf{F}_{\mathcal{C}}^n$  (as well as  $\mathbf{F}_{\mathcal{J}}^n$ ), is derived at time  $t = t_k$ , while the relative velocity  $\mathbf{v}_t$  is evaluated at time  $t = t_{k+1}$ ; all other forces are treated fully implicitly and updated through a classical gradient descent algorithm.

### 3. Results

In this section, numerical examples are solved with our newly-introduced discrete model. The proposed method is implemented with *Eigen* and optimized by compiling with *BLAS* and *LAPACK* backend, and the sparse matrix is solved by *PARDISO* from *Intel's oneAPI Math Kernel Library*

(MKL). A ring slides on a rigid rod is first used to verify our model, and the Young's modulus of 1D rod is reduced to show the nonlinear dynamic interaction between a sliding ring and the deformable structure. Then, two complex examples are analysed to show the effectiveness of our model for practical engineering applications.

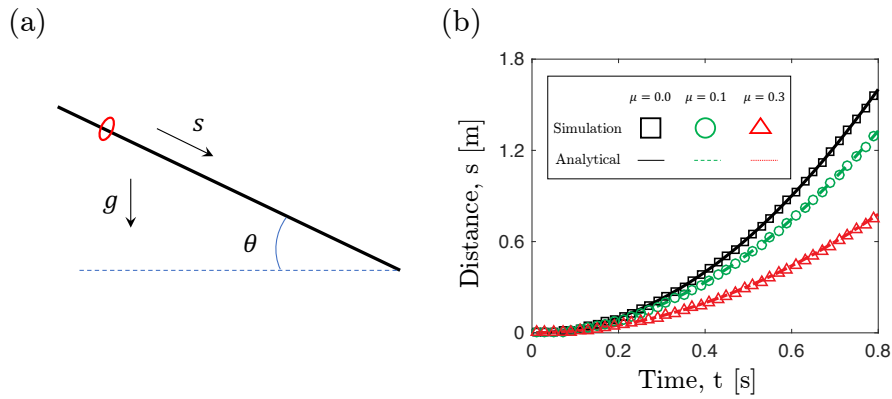


Figure 4: (a) Schematic of a ring sliding on an inclined rod. (b) Translational displacements are plotted against time for both numerical results and analytical solutions.

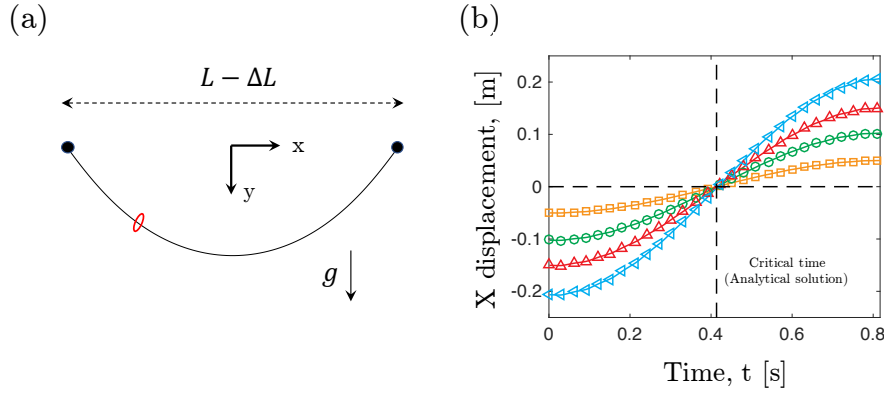


Figure 5: (a) Schematic of a ring slides on an autochrone curve. (b) Displacement along  $x$  direction is plotted against time.

Table 1: Physical and geometric parameters for Sec. 3.1, Sec. 3.2, and Sec. 3.3

Parameters	Notation	Value for Sec. 3.1	Value for Sec. 3.2	Value for Sec. 3.3	Unit
Rod modulus	$E$	1000	1000	{100, 1, 0.01}	GPa
Rod length	$L$	2.0	2.0	2.0	m
Rod radius	$r_0$	10	10	1	mm
Rod density	$\rho$	1000.0	1000.0	1000.0	kg/m <sup>3</sup>
Gravity	$g$	-10.0	-10.0	-10.0	m/s <sup>2</sup>
Ring mass	$m_0$	1	1	1	g
Barrier parameter	$\tilde{d}$	0.01	0.01	0.01	m
Stiffness parameter	$K_{\mathcal{J}}$	1.0	1.0	1.0	N/m
Frictional coefficient	$\mu$	{0.0, 0.1, 0.3}	0.0	{0.0, 0.1, 0.3}	-
Velocity bound	$\epsilon_v$	$10^{-6}$	$10^{-6}$	$10^{-6}$	m/s
Mass damping	$\alpha$	0.00	0.00	0.00	-
Stiffness damping	$\beta$	0.00	0.00	0.01	-

### 3.1. A ring sliding on a rigid inclined bar

The simplest case – a ring sliding on a rigid inclined bar – is considered and compared with analytical solution. Here, we only consider the ring-to-rod interaction because the particle-particle contact does not appear. The problem setup can be referred to Fig. 4(a), the geometric and physical parameters are provided in Table 1. The bar is discretized into 200 nodes, resulting overall DOF vector (rod together with ring)  $\mathbf{q} \in \mathbb{R}^{3 \times 201}$ . The time step size is set to be  $h = 1$  ms, but a larger time step size is also acceptable. The inclined angle is selected as  $\theta = 30^\circ$ . The first node and the last node of the bar are constrained with Dirichlet boundary condition to avoid the rigid body motion. Due to the relatively large bending stiffness, the rod deformation is negligible and the structure is assumed to be rigid.

The point mass would slide along the tangential direction of the inclined

bar if its frictional coefficient is smaller than the threshold, e.g.,  $\mu < \tan \theta$ , and the trajectory of the ring is given by,

$$s = \frac{1}{2}gt^2(\sin \theta - \mu \cos \theta). \quad (13)$$

Fig. 4(b) shows the change of position as a function of time from both numerical data and analytical result. The agreement of lines (analytical solution) and symbols (numerical data) validates the proposed discrete numerical model.

### 3.2. A ring sliding on a rigid tautochrone curve

A more complicated example – one ring sliding on a rigid tautochrone curve – is used for validation, as the analytical solution of which is also available. The shape of tautochrone curve can be achieved by compressing a flexible rod under gravity, and its deformable configuration is a catenary [63]. Referring to Fig. 5(a), a circular ring entangled with a rigid curve is applied, and the function of which is given by,

$$y = A \cosh\left(\frac{x}{A}\right). \quad (14)$$

A tautochrone with arc-length  $L = 2.0$  m is adopted. It has a compressive distance ratio  $\Delta L/L = 20\%$ , and its curvature  $A = 0.6764$  m, thus  $x \in [-0.8, 0.8]$  m. Again, similar to the previous case, the rod is cut into 200 nodes and the first and last node of rod are fixed; The bending stiffness is also enormous to accomplish the structural rigidity.

In Fig. 5(b), we show the  $x$  displacement of the ring evolves as a function of time from our numerical side. Intriguingly, the rings with different start heights,  $y \in \{0.05, 0.10, 0.15, 0.20\}$ , reach the minimum with identical time,

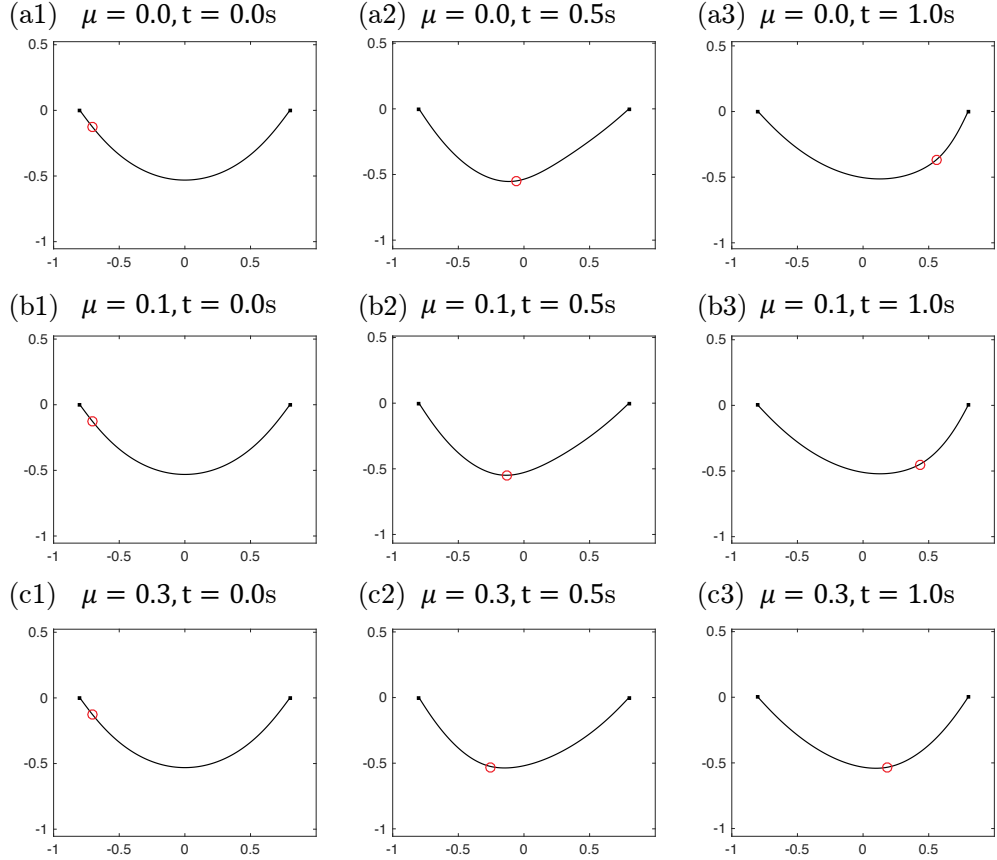


Figure 6: Configurations of a moving mass joint on a flexible rod. Here, the Young's modulus of elastic rod is  $E = 1$  GPa.

$T_{\text{critical}} \sim 0.4085$  s, as the name of Tautochrone curve. The analytical solution of drop time can be derived based on classical calculus of variations,

$$T_{\text{critical}} = \frac{\pi}{2} \sqrt{\frac{A}{g}}. \quad (15)$$

A good agreement has been found for the critical time predicted by numerical simulation and analytical formulation.

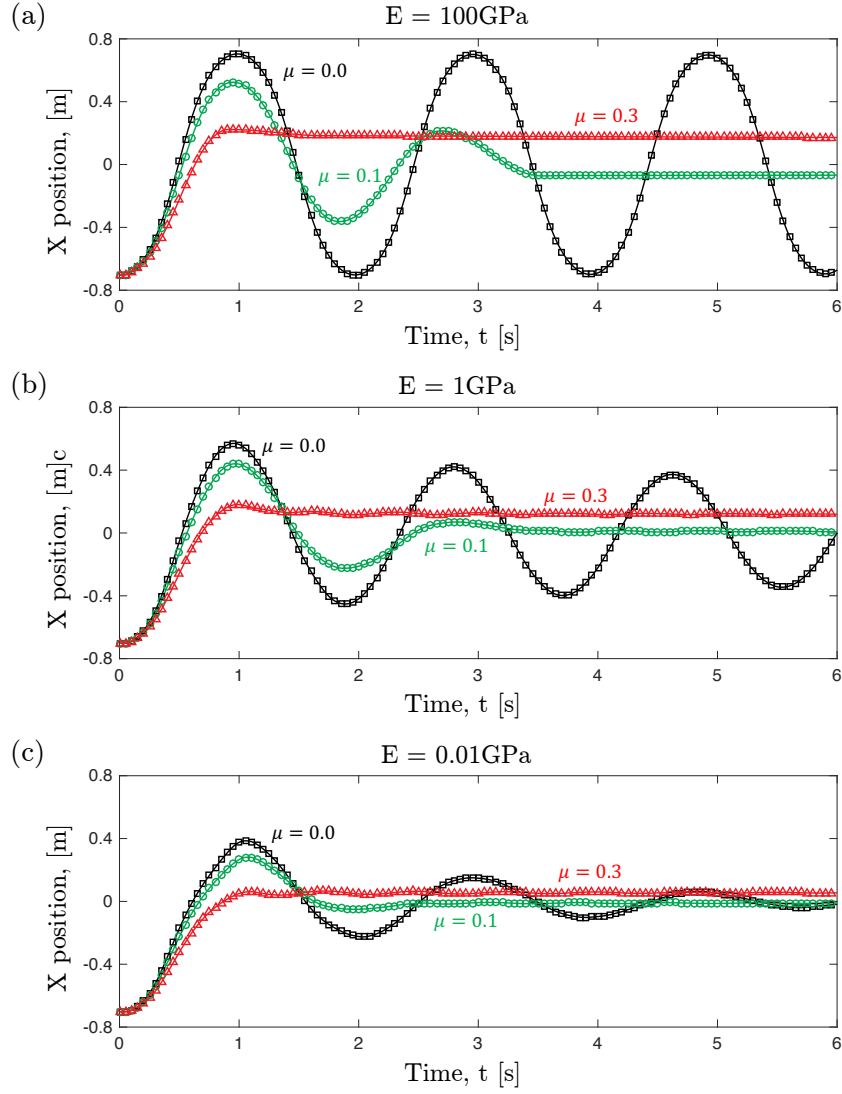


Figure 7: Horizontal position of sliding ring as a function of time. The Young's modulus of elastic rod is varied from  $\{100, 1, 0.01\}$  GPa and the friction coefficients are selected from  $\{0.0, 0.1, 0.3\}$ . The dynamic evolutions are provided in Supplementary Material [Movie\\_S1](#), [Movie\\_S2](#), and [Movie\\_S3](#).

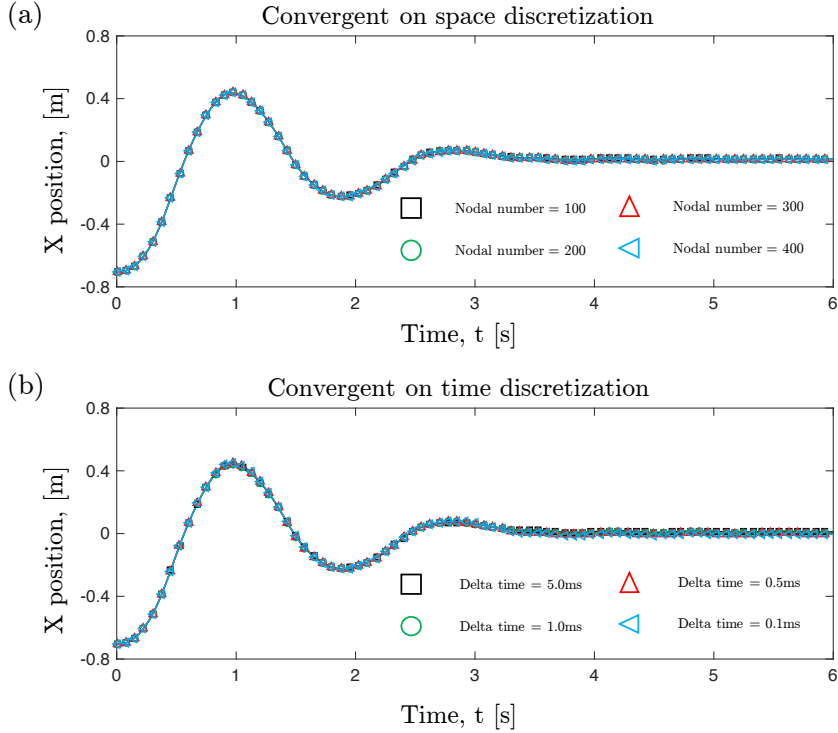


Figure 8: Convergent study. (a) Convergent for space discretization. (b) Convergent for time discretization.

### 3.3. A ring sliding on a flexible tautochrone curve

Similar to the previous example, a rigid ring moving on a tautochrone curve is adopted here, and the only difference is that the bending stiffness of suspended rod is reduced significantly such that the structure changes from rigid to elastic. The geometric and physical parameters are in Table 1. Here, some material damping is added into dynamic system to avoid unrealistic vibratory motion of structure.

The rigid ring is yoked onto the left side of flexible rod and would move to the right due to the existence of gravity, which is similar to the previous

scenario. On the other side, the rod would also be bent as the movement of ring, because the ring can be regarded as a point load onto the curved beam. Snapshots are provided in Fig. 6. In contrast to the previous example, the ring will not move to the same height on the right side if the rod is relatively soft, as some of the gravitational potential is switched to the elastic energy of structure. Moreover, the energy would dissipate faster and the vibratory motion of ring would gradually disappear as the enlarge of frictional coefficient, as expected. Seeing Fig. 7 for more details. The dynamic motions for different frictional coefficients and different rod bending stiffness are provided as Supplementary Material [Movie\\_S1](#), [Movie\\_S2](#), and [Movie\\_S3](#). To

Table 2: Physical and geometric parameters for Sec. 3.4

Parameters	Notation	Value	Unit
Plate modulus	$Y$	0.1	MPa
Rod modulus	$E$	1	MPa
Plate length	$L_P$	0.3	m
Plate width	$W_P$	0.2	m
Plate thickness	$b$	1	mm
Rod length	$L_R$	0.5	m
Rod radius	$r_0$	1	mm
Material density	$\rho$	1000.0	kg/m <sup>3</sup>
Gravity	$g$	-10.0	m/s <sup>2</sup>
Stiffness parameter	$K_J$	100.0	N/m
Barrier parameter	$\tilde{d}$	0.05	m
Frictional coefficient	$\mu$	0.2	-
Velocity bound	$\epsilon_v$	$10^{-6}$	m/s
Mass damping	$\alpha$	0.01	-
Stiffness damping	$\beta$	0.00	-

show the accuracy of our numerical approach, we perform a convergent study in Fig. 8. Here, we use  $E = 1\text{GPa}$  and  $\mu = 0.1$  for demonstration (green curve in Fig. 7(b)). The overlapping curves in both space and time discretizations indicate the correctness of our model.

### 3.4. Hanging clothes

The numerical model is then applied to a more complex case – hanging clothes, which is largely studied in computer graphics community for visual animations [45, 64, 65]. The 2D surface is discretized into multiple triangular meshes and the 1D rod is discretized into several nodes and edges. The physical and geometric parameters for this numerical test are provided in Table 2. The elastic rod is represented by 100 nodes and the flexible cloth is divided into 1402 nodes (and, therefore, 4090 connected edges and 2688 triangular meshes). The first and last two nodes are manually fixed to establish the clamped-clamped boundary condition; all nodes on cloth are free to move and 5 massless rings are used to connect thin cloth and slender rod. It is worth noting that the nodal positions on plate are used directly to represent the sliding rings and no extra vertex is employed to account for coupled joint. The discrete time step size is  $h = 0.1\text{ms}$ .

Initially, the hanging rod would deform from a straight configuration into a curved shape; next, the sliding joint would move towards to the middle as the rod is inclined and the compressive loads are applied back to cloth; Finally, some vivid wrinkles would appear due the high flexibility of elastic cloth under compressive load, seeing Fig. 7(a)-(d) for details. To show the effectiveness of our ring-to-rod model, the constraints on the right side are released at  $t = 1.0\text{ s}$ , such that the clamped-clamped beam would switch to

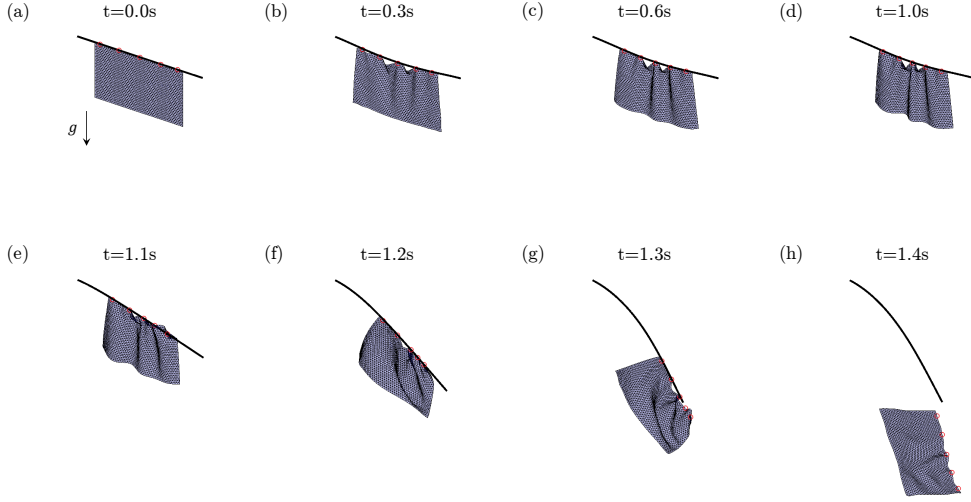


Figure 9: Snapshots of hanging clothes. The dynamic process can be found in Supplementary Material [Movie\\_S4](#).

the clamped-free boundary condition (a cantilever beam model). The hanging cloth would then slide together with the coupled joints from middle to right due to the asymmetric constraints of elastic rod and the external gravitational force; the rings would gradually shed one by one from the slender rods and loss all connections completely after  $t = 1.4$  s, referring to Fig. 7(e)-(h). The overall dynamic process can be found in Supplementary Material [Movie\\_S4](#).

### 3.5. Closing a tether-net

Finally, our numerical model is applied onto the dynamic interaction between tether rod and flexible net through joint rings, in order to realize the net closing mechanism during the debris capture mission [12, 16, 15]. Referring to Fig. 10(a), a rigid object with spherical shape is on top of an elastic net, and the tether rods (coloured by green) for close mechanism are con-

nected with a hexagonal net by multiple rigid rings (coloured by red). The net is discretized into 6931 nodes and 8316 edges; each tether rod (overall 6) is divided by 64 vertex and 63 edges; 8 joint rings are setup for each tether rod. Again, the ring vertex is the same one with the nodes on net and no extra degrees of freedom are required to mimic the mechanics of rings. Here, both ring-to-rod interaction and ball-to-net contact are included into the numerical simulation. The time step size is  $h = 1$  ms, which is identical to the previous numerical examples. All other geometric and physical parameters for this numerical experiments are listed in Table 3.

The overall capture progress can be divided into 3 phases. (i) During  $0s \leq t < 5s$ , the rigid ball and the flexible net would drop under gravity and contact with each other. (ii) When  $5s \leq t < 25s$ , the six corner nodes are manually moved towards center with speed 1.0m/s, until the distance between adjacent corners is smaller than 5.0m, e.g., configurations in Fig. 10(d). (iii) After  $t = 25s$ , the six tether rods are stretched out, and, therefore, the net can be pulled up and partially closed due to the connection through joint rings, referring to Fig. 10(e)-(i). The stretching speed of green tether rods is also set to be 1.0m/s for convenience. The open size of tether-net system after closing can be tuned during phase (ii). The overall ball capture process and net close procedure is provided in Supplementary Material [Movie\\_S5](#).

#### 4. Conclusion

A discrete numerical framework has been developed to study the nonlinear dynamic interaction between a moving ring on an elastic rod. Instead of discretizing the ring into nodes and edges for contact detection and dynamic

Table 3: Physical and geometric parameters for Sec. 3.5

Parameters	Notation	Value	Unit
Net rod modulus	$E_N$	1	GPa
Tether rod modulus	$E_R$	10	GPa
Net size	$L_N$	20.0	m
Tether rod length	$L_R$	20.0	m
Rod radius	$r_0$	1	cm
Material density	$\rho$	1000.0	kg/m <sup>3</sup>
Ball radius	$R_B$	4.0	m
Ball mass	$M_B$	1000	kg
Ball initial height	$H_B$	5.0	m
Gravity	$g$	-10.0	m/s <sup>2</sup>
Stiffness parameter	$K_J$	1000.0	N/m
Barrier parameter	$\tilde{d}$	0.5	m
Stiffness parameter	$K_C$	$10^5$	N/m
Barrier parameter	$\bar{d}$	0.1	m
Frictional coefficient	$\mu$	0.2	-
Velocity bound	$\epsilon_v$	$10^{-6}$	m/s
Mass damping	$\alpha$	0.1	-
Stiffness damping	$\beta$	0.0	-

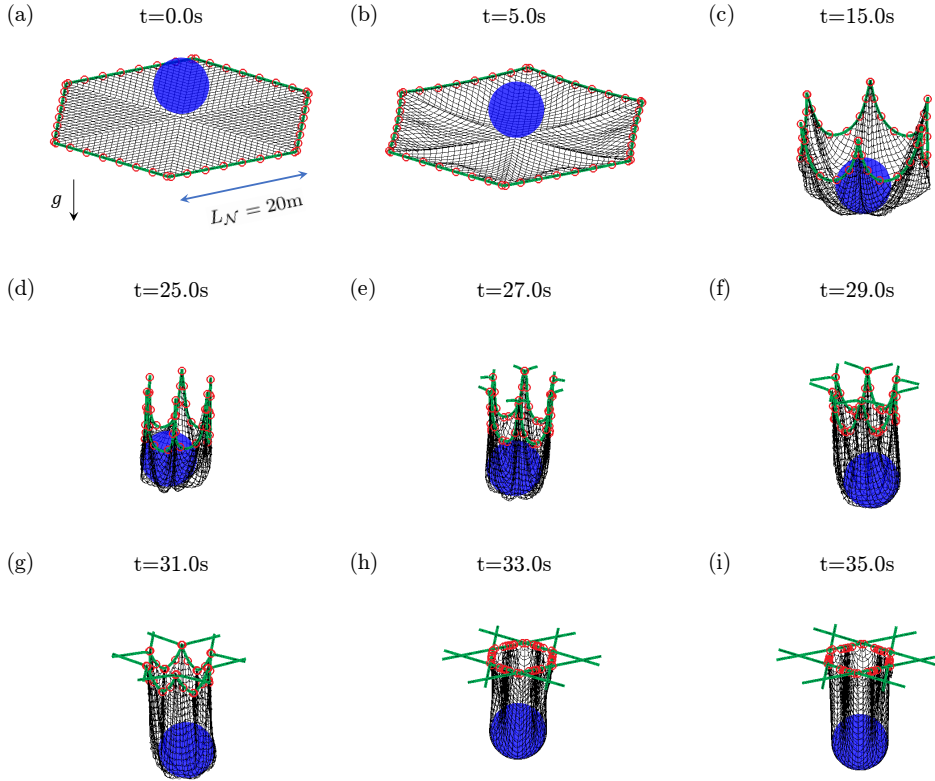


Figure 10: Snapshots of closing a tether-net. The dynamic progress can be found in Supplementary Material [Movie\\_S5](#).

simulation, a single point was used to achieve model order reduction. The non-deviation condition between sliding joint and flexible cable was realized by a novel log-type barrier functional. The frictional interaction along the tangential direction was later included in a manner similar to normal contact force. The proposed functionals were with higher order continuous and could be adopted to solve the nonlinear elastodynamic system through an implicit approach. To verify the proposed method, two simple numerical example were first solved and compared with their analytical solutions. Then, two

examples with large scale systems were considered to demonstrate the effectiveness of the proposed framework for solving practical engineering problems, e.g., cartoon animations in computer graphics and tether-net capture in space debris removal. The implemented ring-to-rod numerical framework could provide eye-catching videos for computer graphics community as well as benefit the optimal design of mechanical engineered systems.

### **Acknowledgments**

This work was supported by the Natural Science Foundation of Jiangsu Province, No. BK20220794.

### **Conflict of interest**

The authors declare that they have no conflict of interest.

### **Availability of data**

The datasets generated during the current study are available from the corresponding author on reasonable request.

### **Availability of Code**

The code generated during the current study are available from the corresponding author on reasonable request.

### **References**

- [1] C. Mote Jr, On the nonlinear oscillation of an axially moving string, Journal of Applied Mechanics 33 (2) (1966) 463–464.

- [2] B. Tabarrok, C. Leech, Y. Kim, On the dynamics of an axially moving beam, *Journal of the Franklin Institute* 297 (3) (1974) 201–220.
- [3] J. Wickert, Non-linear vibration of a traveling tensioned beam, *International Journal of Non-Linear Mechanics* 27 (3) (1992) 503–517.
- [4] X. Zheng, T. Yang, Z. Chen, X. Wang, B. Liang, Q. Liao, Ale formulation for dynamic modeling and simulation of cable-driven mechanisms considering stick–slip frictions, *Mechanical Systems and Signal Processing* 168 (2022) 108633.
- [5] A. Tonoli, E. Zenerino, N. Amati, Modeling the flexural dynamic behavior of axially moving continua by using the finite element method, *Journal of Vibration and Acoustics* 136 (1).
- [6] K. Fu, Z. Zhao, G. Ren, Y. Xiao, T. Feng, J. Yang, P. Gasbarri, From multiscale modeling to design of synchronization mechanisms in mesh antennas, *Acta Astronautica* 159 (2019) 156–165.
- [7] Y. Vetyukov, E. Oborin, J. Scheidl, M. Krommer, C. Schmidrathner, Flexible belt hanging on two pulleys: contact problem at non-material kinematic description, *International Journal of Solids and Structures* 168 (2019) 183–193.
- [8] S. Ma, B. Liang, T. Wang, Dynamic analysis of a hyper-redundant space manipulator with a complex rope network, *Aerospace Science and Technology* 100 (2020) 105768.

- [9] W. Xu, T. Liu, Y. Li, Kinematics, dynamics, and control of a cable-driven hyper-redundant manipulator, *IEEE/ASME Transactions on Mechatronics* 23 (4) (2018) 1693–1704.
- [10] J. Lim, J. Chung, Dynamic analysis of a tethered satellite system for space debris capture, *Nonlinear Dynamics* 94 (4) (2018) 2391–2408.
- [11] Y. Chen, R. Huang, L. He, X. Ren, B. Zheng, Dynamical modelling and control of space tethers: a review of space tether research, *Nonlinear Dynamics* 77 (4) (2014) 1077–1099.
- [12] E. M. Botta, I. Sharf, A. K. Misra, M. Teichmann, On the simulation of tether-nets for space debris capture with vortex dynamics, *Acta Astronautica* 123 (2016) 91–102.
- [13] E. M. Botta, I. Sharf, A. K. Misra, Simulation of tether-nets for capture of space debris and small asteroids, *Acta Astronautica* 155 (2019) 448–461.
- [14] M. Shan, J. Guo, E. Gill, Contact dynamic models of space debris capturing using a net, *Acta Astronautica* 158 (2019) 198–205.
- [15] Y. Hou, C. Liu, H. Hu, W. Yang, J. Shi, Dynamic computation of a tether-net system capturing a space target via discrete elastic rods and an energy-conserving integrator, *Acta Astronautica* 186 (2021) 118–134.
- [16] I. Sharf, B. Thomsen, E. M. Botta, A. K. Misra, Experiments and simulation of a net closing mechanism for tether-net capture of space debris, *Acta Astronautica* 139 (2017) 332–343.

- [17] E. M. Botta, C. Miles, I. Sharf, Simulation and tension control of a tether-actuated closing mechanism for net-based capture of space debris, *Acta Astronautica* 174 (2020) 347–358.
- [18] W. Huang, D. He, D. Zhang, H. Zou, H. Liu, W. Yang, L. Qin, Q. Fei, Nonlinear dynamic modeling of a tether-net system for space debris capture, *Nonlinear Dynamics*.
- [19] T. J. Hughes, *The finite element method: linear static and dynamic finite element analysis*, Courier Corporation, 2012.
- [20] V. Sonnevile, A. Cardona, O. Brüls, Geometrically exact beam finite element formulated on the special euclidean group  $se(3)$ , *Computer Methods in Applied Mechanics and Engineering* 268 (2014) 451–474.
- [21] H. Farokhi, Y. Xia, A. Erturk, Experimentally validated geometrically exact model for extreme nonlinear motions of cantilevers, *Nonlinear Dynamics* 107 (1) (2022) 457–475.
- [22] A. A. Shabana, An absolute nodal coordinate formulation for the large rotation and deformation analysis of flexible bodies, Technical Report, Department of Mechanical Engineering, University of Illinois at Chicago.
- [23] A. A. Shabana, R. Y. Yakoub, Three dimensional absolute nodal coordinate formulation for beam elements: theory, *J. Mech. Des.* 123 (4) (2001) 606–613.
- [24] R. Y. Yakoub, A. A. Shabana, Three dimensional absolute nodal coordinate formulation for beam elements: implementation and applications, *J. Mech. Des.* 123 (4) (2001) 614–621.

- [25] J. Kiendl, F. Auricchio, L. B. da Veiga, C. Lovadina, A. Reali, Isogeometric collocation methods for the reissner–mindlin plate problem, *Computer Methods in Applied Mechanics and Engineering* 284 (2015) 489–507.
- [26] I. Steinbrecher, A. Humer, L. Vu-Quoc, On the numerical modeling of sliding beams: a comparison of different approaches, *Journal of Sound and Vibration* 408 (2017) 270–290.
- [27] S. Han, Configurational forces and geometrically exact formulation of sliding beams in non-material domains, *Computer Methods in Applied Mechanics and Engineering* 395 (2022) 115063.
- [28] H. Irschik, H. Holl, The equations of lagrange written for a non-material volume, *Acta Mechanica* 153 (3) (2002) 231–248.
- [29] C. Pesce, The application of lagrange equations to mechanical systems with mass explicitly dependent on position, *J. Appl. Mech.* 70 (5) (2003) 751–756.
- [30] A. Humer, I. Steinbrecher, L. Vu-Quoc, General sliding-beam formulation: A non-material description for analysis of sliding structures and axially moving beams, *Journal of Sound and Vibration* 480 (2020) 115341.
- [31] F. Boyer, V. Lebastard, F. Candelier, F. Renda, Extended hamilton’s principle applied to geometrically exact kirchhoff sliding rods, *Journal of Sound and Vibration* 516 (2022) 116511.
- [32] G. Fotland, B. Haugen, Numerical integration algorithms and constraint

formulations for an ale-ancf cable element, *Mechanism and Machine Theory* 170 (2022) 104659.

- [33] J. J. Muñoz, G. Jelenić, Sliding contact conditions using the master–slave approach with application on geometrically non-linear beams, *International journal of solids and structures* 41 (24–25) (2004) 6963–6992.
- [34] S.-H. Lee, T.-W. Park, J.-H. Seo, J.-W. Yoon, K.-J. Jun, The development of a sliding joint for very flexible multibody dynamics using absolute nodal coordinate formulation, *Multibody System Dynamics* 20 (3) (2008) 223–237.
- [35] D. Hong, G. Ren, A modeling of sliding joint on one-dimensional flexible medium, *Multibody System Dynamics* 26 (1) (2011) 91–106.
- [36] J. Guo, Y. Zhang, C. Wei, Y. Zhao, Energy–momentum integration and analysis for sliding contact coupling dynamics in large flexible multibody system, *Nonlinear Dynamics*.
- [37] W. Huang, X. Huang, C. Majidi, M. K. Jawed, Dynamic simulation of articulated soft robots, *Nature communications* 11 (1) (2020) 1–9.
- [38] M. K. Jawed, N. Khouri, F. Da, E. Grinspun, P. M. Reis, Propulsion and instability of a flexible helical rod rotating in a viscous fluid, *Physical review letters* 115 (16) (2015) 168101.
- [39] E. Grinspun, M. Desbrun, K. Polthier, P. Schröder, A. Stern, Discrete differential geometry: an applied introduction, *ACM SIGGRAPH Course* 7 (2006) 1–139.

- [40] M. Bergou, M. Wardetzky, S. Robinson, B. Audoly, E. Grinspun, Discrete elastic rods, in: ACM transactions on graphics (TOG), Vol. 27, ACM, 2008, p. 63.
- [41] M. Bergou, B. Audoly, E. Vouga, M. Wardetzky, E. Grinspun, Discrete viscous threads, in: ACM Transactions on Graphics (TOG), Vol. 29, ACM, 2010, p. 116.
- [42] Z. Shen, J. Huang, W. Chen, H. Bao, Geometrically exact simulation of inextensible ribbon, in: Computer Graphics Forum, Vol. 34, Wiley Online Library, 2015, pp. 145–154.
- [43] W. Huang, C. Ma, L. Qin, Snap-through behaviors of a pre-deformed ribbon under midpoint loadings, International Journal of Solids and Structures (2021) 111184.
- [44] W. Huang, C. Ma, Q. Chen, L. Qin, A discrete differential geometry-based numerical framework for extensible ribbons, International Journal of Solids and Structures 248 (2022) 111619.
- [45] D. Baraff, A. Witkin, Large steps in cloth simulation, in: Proceedings of the 25th annual conference on Computer graphics and interactive techniques, ACM, 1998, pp. 43–54.
- [46] D. House, D. Breen, Cloth modeling and animation, CRC Press, 2000.
- [47] W. Huang, Y. Wang, X. Li, M. K. Jawed, Shear induced supercritical pitchfork bifurcation of pre-buckled bands, from narrow strips to wide plates, Journal of the Mechanics and Physics of Solids 145 (2020) 104168.

[48] J. Panetta, M. Konaković-Luković, F. Isvoranu, E. Bouleau, M. Pauly, X-shells: A new class of deployable beam structures, *ACM Transactions on Graphics (TOG)* 38 (4) (2019) 83.

[49] W. Huang, L. Qin, M. Khalid Jawed, Numerical method for direct solution to form-finding problem in convex gridshell, *Journal of Applied Mechanics* 88 (2) (2021) 021012.

[50] W. Huang, L. Qin, Q. Chen, Natural frequencies of pre-buckled rods and gridshells, *Applied Mathematical Modelling* 107 (2022) 621–636.

[51] M. K. Jawed, F. Da, J. Joo, E. Grinspun, P. M. Reis, Coiling of elastic rods on rigid substrates, *Proceedings of the National Academy of Sciences* 111 (41) (2014) 14663–14668.

[52] V. Romero, M. Ly, A.-H. Rasheed, R. Charrondière, A. Lazarus, S. Neukirch, F. Bertails-Descoubes, Physical validation of simulators in computer graphics: A new framework dedicated to slender elastic structures and frictional contact, *ACM Transactions on Graphics*.

[53] C. Baek, A. O. Sageman-Furnas, M. K. Jawed, P. M. Reis, Form finding in elastic gridshells, *Proceedings of the National Academy of Sciences* 115 (1) (2018) 75–80.

[54] M. Li, Z. Ferguson, T. Schneider, T. R. Langlois, D. Zorin, D. Panozzo, C. Jiang, D. M. Kaufman, Incremental potential contact: intersection- and inversion-free, large-deformation dynamics., *ACM Trans. Graph.* 39 (4) (2020) 49.

- [55] M. Li, D. M. Kaufman, C. Jiang, Codimensional incremental potential contact, arXiv preprint arXiv:2012.04457.
- [56] A. Choi, D. Tong, M. K. Jawed, J. Joo, Implicit contact model for discrete elastic rods in knot tying, *Journal of Applied Mechanics* 88 (5).
- [57] Q. Li, T. Wang, V. Roychowdhury, M. K. Jawed, Rapidly encoding generalizable dynamics in a euclidean symmetric neural network: a slinky case study, arXiv preprint arXiv:2203.11546.
- [58] D. Tong, A. Choi, J. Joo, M. K. Jawed, A fully implicit method for robust frictional contact handling in elastic rods, arXiv preprint arXiv:2205.10309.
- [59] J. J. Moreau, On unilateral constraints, friction and plasticity, in: *New variational techniques in mathematical physics*, Springer, 2011, pp. 171–322.
- [60] H. Liang, L. Mahadevan, The shape of a long leaf, *Proceedings of the National Academy of Sciences* 106 (52) (2009) 22049–22054.
- [61] T. Savin, N. A. Kurpios, A. E. Shyer, P. Florescu, H. Liang, L. Mahadevan, C. J. Tabin, On the growth and form of the gut, *Nature* 476 (7358) (2011) 57.
- [62] W. Huang, M. K. Jawed, Newmark-beta method in discrete elastic rods algorithm to avoid energy dissipation, *Journal of Applied Mechanics* 86 (8).

- [63] W. Huang, D. He, D. Tong, Y. Chen, X. Huang, L. Qin, Q. Fei, Static analysis of elastic cable structures under mechanical load using discrete catenary theory, *Fundamental Research*.
- [64] K.-J. Choi, H.-S. Ko, Research problems in clothing simulation, *Computer-aided design* 37 (6) (2005) 585–592.
- [65] R. Bridson, S. Marino, R. Fedkiw, Simulation of clothing with folds and wrinkles, in: *ACM SIGGRAPH 2005 Courses*, ACM, 2005, p. 3.